

Simultaneous space and phase resolved X-ray polarimetry of the Crab Pulsar and Nebula

Niccolò Bucciantini^{1,2,3*}, Riccardo Ferrazzoli⁴, Matteo Bachetti⁵, John Rankin⁴, Niccolò Di Lalla⁶, Carmelo Sgrò⁷, Nicola Omodei⁶, Takao Kitaguchi⁸, Tsunefumi Mizuno⁹, Shuichi Gunji¹⁰, Eri Watanabe¹⁰, Luca Baldini^{7,11}, Patrick Slane¹², Martin C. Weisskopf¹³, Roger W. Romani⁶, Andrea Possenti⁵, Herman L. Marshall¹⁴, Stefano Silvestri⁷, Luigi Pacciani⁴, Michela Negro^{15,16,17}, Fabio Muleri⁴, Emma de Oña Wilhelmi¹⁸, Fei Xie^{19,4}, Jeremy Heyl²⁰, Melissa Pesce-Rollins⁷, Josephine Wong⁶, Maura Pilia⁵, Iván Agudo²¹, Lucio A. Antonelli^{22,23}, Wayne H. Baumgartner¹³, Ronaldo Bellazzini⁷, Stefano Bianchi²⁴, Stephen D. Bongiorno¹³, Raffaella Bonino^{25,26}, Alessandro Brez⁷, Fiamma Capitanio⁴, Simone Castellano⁷, Elisabetta Cavazzuti²⁷, Chien-Ting Chen²⁸, Stefano Ciprini^{29,23}, Enrico Costa⁴, Alessandra De Rosa⁴, Ettore Del Monte⁴, Laura Di Gesu²⁷, Alessandro Di Marco⁴, Immacolata Donnarumma²⁷, Victor Doroshenko³⁰, Michal Dovčiak³¹, Steven R. Ehlert¹³, Teruaki Enoto⁸, Yuri Evangelista⁴, Sergio Fabiani⁴, Javier A. Garcia³², Kiyoshi Hayashida³³, Wataru Iwakiri³⁴, Svetlana G. Jorstad^{35,36}, Philip Kaaret³⁷, Vladimir Karas³¹, Fabian Kislak³¹, Jeffery J. Kolodziejczak¹³, Henric Krawczynski³⁸, Fabio La Monaca⁴, Luca Latronico²⁵, Ioannis Liodakis³⁹, Simone Maldera²⁵, Alberto Manfreda⁷, Frédéric Marin⁴⁰, Andrea Marinucci²⁷, Alan P. Marscher³⁵, Francesco Massaro^{25,26}, Giorgio Matt²⁴, Ikuyuki Mitsuishi⁴¹, C.-Y. Ng⁴², Stephen L. O'Dell¹³, Chiara Oppedisano²⁵, Alessandro Papitto²², George G. Pavlov⁴³, Abel L. Peirson⁶, Matteo Perri^{22,23}, Pierre-Olivier Petrucci⁴⁴, Juri

Poutanen⁴⁵, Simonetta Puccetti²³, Brian D. Ramsey¹³, Ajay Ratheesh⁴, Oliver Roberts²⁸, Paolo Soffitta⁴, Gloria Spandre⁷, Doug Swartz⁵⁰, Toru Tamagawa⁸, Fabrizio Tavecchio⁴⁶, Roberto Taverna⁴⁷, Yuzuru Tawara⁴¹, Allyn F. Tennant¹³, Nicolas E. Thomas¹³, Francesco Tombesi^{48,28,17}, Alessio Trois⁵, Sergey Tsygankov⁴⁵, Roberto Turolla^{47,49}, Jacco Vink⁵⁰, Kinwah Wu⁴⁹ and Silvia Zane⁴⁹

¹INAF Osservatorio Astrofisico di Arcetri, Largo Enrico Fermi 5, 50125 Firenze, Italy.

²Dipartimento di Fisica e Astronomia, Università degli Studi di Firenze, Via Sansone 1, 50019 Sesto Fiorentino (FI), Italy.

³Istituto Nazionale di Fisica Nucleare, Sezione di Firenze, Via Sansone 1, 50019 Sesto Fiorentino (FI), Italy.

⁴INAF Istituto di Astrofisica e Planetologia Spaziali, Via del Fosso del Cavaliere 100, 00133 Roma, Italy.

⁵INAF Osservatorio Astronomico di Cagliari, Via della Scienza 5, 09047 Selargius (CA), Italy.

⁶Department of Physics and Kavli Institute for Particle Astrophysics and Cosmology, Stanford University, Stanford, California 94305, USA..

⁷Istituto Nazionale di Fisica Nucleare, Sezione di Pisa, Largo B. Pontecorvo 3, 56127 Pisa, Italy.

⁸RIKEN Cluster for Pioneering Research, 2-1 Hirosawa, Wako, Saitama 351-0198, Japan .

⁹Hiroshima Astrophysical Science Center, Hiroshima University, 1-3-1 Kagamiyama, Higashi-Hiroshima, Hiroshima 739-8526, Japan .

¹⁰Yamagata University, 1-4-12 Kojirakawa-machi, Yamagata-shi 990-8560, Japan.

¹¹Dipartimento di Fisica, Università di Pisa; Largo B. Pontecorvo 3, 56127 Pisa, Italy.

¹²Center for Astrophysics, Harvard Smithsonian; 60 Garden St, Cambridge, MA 02138, USA.

¹³NASA Marshall Space Flight Center; Huntsville, AL 35812, USA.

¹⁴MIT Kavli Institute for Astrophysics and Space Research, Massachusetts Institute of Technology; 77 Massachusetts Avenue, Cambridge, MA 02139, USA.

- ¹⁵Center for Research and Exploration in Space Science and Technology, NASA/GSFC; Greenbelt, MD 20771, USA.
- ¹⁶NASA Goddard Space Flight Center; Greenbelt, MD 20771, USA.
- ¹⁷Department of Astronomy, University of Maryland; College Park, Maryland 20742, USA..
- ¹⁸Deutsches Elektronen-Synchrotron (DESY), 15738 Zeuthen, Germany.
- ¹⁹Guangxi Key Laboratory for Relativistic Astrophysics, School of Physical Science and Technology; Guangxi University, Nanning 530004, China.
- ²⁰University of British Columbia; Vancouver, BC V6T 1Z4, Canada.
- ²¹Instituto de Astrofísica de Andalucía, IAA-CSIC; Glorieta de la Astronomía s/n, 18008 Granada, Spain.
- ²²INAF Osservatorio Astronomico di Roma, Via Frascati 33, 00078 Monte Porzio Catone, Roma, Italy.
- ²³Space Science Data Center, Agenzia Spaziale Italiana, Via del Politecnico snc, 00133 Roma, Italy.
- ²⁴Dipartimento di Matematica e Fisica, Università degli Studi Roma Tre; Via della Vasca Navale 84, 00146 Roma, Italy.
- ²⁵Istituto Nazionale di Fisica Nucleare, Sezione di Torino; Via Pietro Giuria 1, 10125 Torino, Italy.
- ²⁶Dipartimento di Fisica, Università degli Studi di Torino; Via Pietro Giuria 1, 10125 Torino, Italy.
- ²⁷ASI - Agenzia Spaziale Italiana; Via del Politecnico snc 00133 Roma, Italy.
- ²⁸Science and Technology Institute, Universities Space Research Association, Huntsville, AL 35805, USA.
- ²⁹Istituto Nazionale di Fisica Nucleare, Sezione di Roma “Tor Vergata”; Via della Ricerca Scientifica 1, 00133 Roma, Italy.
- ³⁰Institut für Astronomie und Astrophysik, Universität Tübingen; Sand 1, 72076 Tübingen, Germany.
- ³¹Astronomical Institute of the Czech Academy of Sciences; Bořm II 1401/1, 14100 Praha 4, Czech Republic.
- ³²California Institute of Technology; Pasadena, CA 91125, USA.
- ³³Osaka University; 1-1 Yamadaoka, Suita, Osaka 565-0871, Japan.

³⁴Department of Physics, Faculty of Science and Engineering, Chuo University; 1-13-27 Kasuga, Bunkyo-ku, Tokyo 112-8551, Japan.

³⁵Institute for Astrophysical Research, Boston University; 725 Commonwealth Avenue, Boston, MA 02215, USA.

³⁶Department of Astrophysics, St. Petersburg State University; Universitetsky pr. 28, Petrodvoretz, 198504 St. Petersburg, Russia.

³⁷Department of Physics and Astronomy, University of Iowa, Iowa City, IA 52242, USA.

³⁸Physics Department and McDonnell Center for the Space Sciences; Washington University in St. Louis, St. Louis, MO 63130, USA.

³⁹Finnish Centre for Astronomy with ESO; 20014 University of Turku, Finland.

⁴⁰Université de Strasbourg, CNRS, Observatoire Astronomique de Strasbourg; UMR 7550, 67000 Strasbourg, France.

⁴¹Graduate School of Science, Division of Particle and Astrophysical Science; Nagoya University, Furo-cho, Chikusa-ku, Nagoya, Aichi 464-8602, Japan.

⁴²Department of Physics, The University of Hong Kong; Pokfulam, Hong Kong.

⁴³Department of Astronomy and Astrophysics, Pennsylvania State University; University Park, PA 16802, USA.

⁴⁴Université Grenoble Alpes, CNRS, IPAG; 38000 Grenoble, France.

⁴⁵Department of Physics and Astronomy, 20014 University of Turku; Finland.

⁴⁶INAF Osservatorio Astronomico di Brera; Via E. Bianchi 46, 23807 Merate (LC), Italy.

⁴⁷Dipartimento di Fisica e Astronomia, Università degli Studi di Padova; Via Marzolo 8, 35131 Padova, Italy.

⁴⁸Dipartimento di Fisica, Università degli Studi di Roma “Tor Vergata”; Via della Ricerca Scientifica 1, 00133 Roma, Italy.

⁴⁹Mullard Space Science Laboratory, University College London; Holmbury St Mary, Dorking, Surrey RH5 6NT, UK.

⁵⁰Anton Pannekoek Institute for Astronomy & GRAPPA, University of Amsterdam; Science Park 904, 1098 XH Amsterdam, The Netherlands.

*Corresponding author(s). E-mail(s): niccolo.bucciantini@inaf.it;

Abstract

The Crab pulsar and its nebula are among the most studied astrophysical systems, and constitute one of the most promising environments where high energy processes and particle acceleration can be investigated. They are the only objects for which significant X-ray polarisation was detected in the past. We present here the Imaging X-ray Polarimetry Explorer (IXPE) observation of the Crab pulsar and nebula. The total pulsar pulsed emission in the [2–8] keV energy range is unpolarised. Significant polarisation up to 15% is detected for the first time in the core of the main peak. The nebula has a total space integrated polarised degree of 20% and polarisation angle of 145° . The polarised maps show a large variation in the local polarisation, and regions with polarised degree up to 45-50%. The polarisation pattern suggests a predominantly toroidal magnetic field. Our findings for the pulsar are inconsistent with the vast majority of inner magnetospheric models, and suggest emission comes more likely from the wind region. For the nebula, the polarization map suggests a patchy distribution of turbulence, uncorrelated with the intensity, in contrast with simple expectations from numerical models.

Keywords: X-rays: general, polarization, supernova remnants, pulsars: individual (Crab)

1 Introduction

The Crab pulsar (PSR B0531+21, PSR J0534+2200) and nebula (G184.6-5.8), born out of the supernova SN1054, form one of the most interesting high energy astrophysical systems, and one of the foremost environments where the physics of compact objects, particle acceleration, and relativistic outflows can be investigated [1, 2].

The Crab pulsar (PSR) and nebula (PWN) are the only astrophysical system for which statistically significant integrated and/or phase-resolved X-ray polarisation was reported in the past by various instruments [3–11], suggesting that the polarisation degree (PD) in the pulses, $\sim 20\%$, is lower than in the interpulse. The integrated X-ray PD in the off pulse (OP) due to the PWN is consistently found to be $\sim 20\%$ with typical polarisation angle (PA) $\sim 130^\circ$ - 140° . The PWN polarimetry by OSO-8 has $PD = 19.19\% \pm 0.97\%$ and $19.50\% \pm 2.77\%$ at 2.6 keV and 5.5 keV respectively, while $PA = 156.36^\circ \pm 1.44^\circ$ and $152.99^\circ \pm 4.04^\circ$, at the same energies [3] (all errors hereafter are at 1σ confidence level, see also the Methods).

The Crab PWN has an apparent size of $6' \times 4'$ in the optical band, about

twice larger than in X-rays, corresponding to about 11×7 ly at its estimated distance of 2 kpc [12]. It has a broad band non-thermal spectrum, extending from radio to TeV energies, due to synchrotron from high energy electrons and positrons up to ~ 150 MeV, and Inverse Compton above. The [2-8] keV integrated luminosity is $\sim 1.8 \times 10^{-8}$ erg cm⁻² s⁻¹ [13] with a photon index $\sim 2.12 - 2.15$ [14]. X-ray imaging shows a well developed axisymmetric structure known as jet-torus [15, 16]. Radio polarisation shows typical average values of the PD in the range 5-10%, and PA = 150°, with no correlation with the X-ray features [17]. High resolution optical polarimetry of few selected features in the inner region, within 10 arcsec from the PSR, shows a PD = 40% and PA = 127° [18].

The Crab PSR has a rotation period $P = 33.7$ ms, and spins down at a rate $\dot{P} = 4.21 \times 10^{-13}$ s s⁻¹, corresponding to an effective surface dipole magnetic field of 3.8×10^{12} G, and a spin-down luminosity $\dot{E} = 4.3 \times 10^{38}$ erg s⁻¹ [2]. Pulsed emission has been observed at all wavelengths from radio up to TeV. The pulse shape is characterized by a main pulse (P1), and an interpulse or second pulse (P2), whose positions in phase show only a slight variation with energy [19]. At optical frequencies and above, a bridge (B) of emission is observed between them. The total unabsorbed pulsed X-ray flux in the [2-10] keV band is $\sim 2.7 \times 10^{-9}$ erg cm⁻² s⁻¹ [20], while the photon index in the energy band [1-100] keV is found to vary in phase between 1.4 and 2.2 [21–24]. The photon index is phase dependent: the emission is harder for B than for the peaks, and slightly harder for P2 than P1. Optical and radio polarisation have been measured since the PSR discovery. The OP emission (in optical in the phase range 0.78-0.84) has a PD = 33%, and PA = 130° [25]. After OP subtraction the average PD of the pulses is found to be 5.5% and the average PA is 96° [25].

2 Results

The Imaging X-ray Polarimetry Explorer (IXPE), the first mission devoted to spatially-resolved polarisation measurements in the X-rays [26, 27], was successfully launched on 2021 December 9. IXPE observed the Crab PWN & PSR complex two times between February 21st and March 7th 2022 for a total on-source time of ~ 92 ks. Data were extracted and analysed according to standard procedures: HEASOFT 6.30.1 (<https://heasarc.gsfc.nasa.gov/docs/software/heasoft/>) was used to perform barycenter correction, with the BARYCORR FT00L, using the most recent optical coordinates from the Gaia DATA release 3 (<https://www.cosmos.esa.int/web/gaia/dr3>), the DE421 JPL ephemeris and the ICRS reference frame (see Supplementary Table 1). ixpeobssim V26.3.2 was used to do energy calibration, detector WCS correction, aspect-solution

corrections, and all further (unweighted) analysis [28, 29], including phase folding at the derived ephemeris. We also performed a coeval observation of the Crab PWN with the CHANDRA Satellite (ObsID 23539, see the Methods for further details).

In Figure 1 (see also Table 1) we show the polarised properties of the Crab complex derived by spatially integrating all emission in a region within 2.5 arcmin from the PSR. Background contamination within this region is negligible. There is a significant change in the PA between the low [2-4] keV and high [4-8] keV energy band. The same trend is seen for the OP emission (whose phase range can be found in see Supplementary Table 2), suggesting that it is of nebular origin. The change in PD is less significant, with the higher energy band being slightly more polarised. The OP phase emission is marginally more polarised than the total PWN & PSR emission, as already suggested by a similar analysis of the OSO-8 data [3], while there is no evidence for even a marginal change in PA, suggesting that the PSR has a net low level of polarisation, acting mostly to reduce the total level of polarisation. The contribution of the PSR unpulsed (DC) emission [30] to the total OP emission, is estimated to be less than 1%, and we can safely assume that the OP is mostly of nebular origin (we found no evidence for variations of the polarization properties in the OP, see also Supplementary Figure 1). The OP polarisation angle is $\sim 145^\circ$, larger by $\sim 20^\circ$ with respect to the values reported in the literature for the PWN symmetry axis, derived from fitting the X-ray jet-torus intensity maps [26, 31]. It is also smaller by $\sim 10^\circ$ than the previous OSO-8 measurements at a statistically significant level (see the Supplementary Figure 2). Such discrepancies might simply reflect the variability of the PWN, where structures are known to change in shape and location over a typical timescale of a few years [32].

In Figure 2 we show an intensity map of the Crab PWN from the coeval CHANDRA ObsID 23539, the IXPE count map for the PWN+PSR complex in the [2-8] keV energy range, and the IXPE count map in the same energy range, but computed just for the OP emission.

For the phase-resolved analysis of the PSR we take events in the range [2-8] keV and within 20 arcsec from the PSR itself to limit the PWN contamination. The Stokes parameters of the OP emission have been subtracted (see the Supplementary Material for the exact definition of the off pulse in terms of pulse phase, as well as the other phase bins). In Figure 3 we plot the OP-subtracted light curve, in 200 equally spaced phase bins. For the polarisation analysis of the PSR emission we opted for a variable phase binning, focusing on the peaks and bridge, in order to get a finer sampling near P1 and P2. Figure 3 shows PSR normalised Stokes parameters U/I and Q/I, for the phase bins of interest (see the Supplementary Table 2 for further details). The OP emission in the pulsar aperture has $Q/I = -0.0106 \pm 0.008$, $U/I =$

-0.241 ± 0.008 , corresponding to $PD = 24.1\% \pm 0.8\%$ and $PA = 133.6^\circ \pm 1.0^\circ$. This is significantly more polarised than the OP emission for the entire PWN, and the PA is $\sim 10^\circ$ smaller, indicative of a spatial variation of the polarisation properties. The only phase bin showing a polarisation above the 3σ confidence level is the center of P1 in the phase range $[0.12, 0.14]$, where the OP subtracted emission has $Q/I = -0.132 \pm 0.025$, $U/I = -0.079 \pm 0.025$, corresponding to $PD = 15.4\% \pm 2.5\%$ and $PA = 105^\circ \pm 18^\circ$. There is no significant change of the polarisation properties of this phase bin with energy. Rapid PA variation might suppress the polarisation in these bins. The total PSR normalised Stokes parameters are $Q/I = -0.018 \pm 0.019$ and $U/I = -0.019 \pm 0.019$, confirming that the integrated PSR contribution serves only to reduce the polarisation of the entire complex.

In Figure 4 we show the total PWN & PSR map of PD in the [2-8] keV energy range, obtained by smoothing the maps of Stokes parameters with a Gaussian kernel (5 arcsec width), and cut at the 5σ significance level (see the Supplementary Figures 2 and 3), together with an intensity map where we have overlaid the polarised magnetic field direction (by definition perpendicular to direction of the electric field). For the first time we are able to map the magnetic field structure in the inner nebula. The overall polarisation pattern confirms long held general expectations for PWNe, based on the paradigm that the synchrotron emission takes place in the (mostly) toroidal magnetic field, originating from the pulsar wind and compressed in the nebula, which sets the symmetry axis of the jet-torus structure. The observed polarisation and emission patterns arise from the interplay of the magnetic field geometry and bulk motion of the relativistic plasma within the nebula itself, depending also on the inclination of the nebular axis with respect to the line of sight. It is indeed the presence of bulk motions directed toward and away from the observer that creates the various bright arc-like features and makes the front side of the torus brighter than the back. The results shown in Figure 4 agree with this picture, assuming a symmetry axis inclined in the plane of the sky as derived from X-rays [31]. The direction of the inferred magnetic field broadly follows the shape of the emission torus (which extends also on the back but is fainter due to Doppler de-boosting). There are two unpolarised regions at the NE and SW edges of the main torus, where the polarised direction varies rapidly within the point spread function. The overall PD map shows a far stronger level of asymmetry with respect to the PWN axis than the total intensity map, indicating possibly large variations in the amount of magnetic turbulence within the PWN, or major distortions of the magnetic field structure in the fainter outer regions. The more polarised regions are not found in the center of the PWN, where there is a marginal contribution from the PSR that lowers the PD, but north and south of the main torus, in regions that do not correspond to any bright feature in X-ray. Based on smoothed maps the peak PD in the Northern region is found to be 46%, with a PA of 163° , at 25σ significance, while the peak in the southern region has PD of 51%, with a PA

156° at 20 σ significance (see Supplementary Figure 3). Considering instead two circular regions of 15 arcsec radius centered on the polarisation maxima, we found for the northern region integrated quantities: $Q/I = 0.37 \pm 0.01$ and $U/I = -0.25 \pm 0.01$, corresponding to PD 45% \pm 1% and PA 163.3° \pm 0.8°, at 35 σ significance with a Minimum Detectable Polarisation (MDP) at 99% confidence level of 0.04, while the Southern region has $Q/I = 0.30 \pm 0.02$, $U/I = -0.37 \pm 0.02$, corresponding to PD 47% \pm 2% and PA = 154° \pm 1°, at 27 σ significance with a MDP of 0.05. These regions are far enough from the PSR that its depolarising contribution is negligible.

3 Discussion

We report here the first simultaneous phase- and space-resolved soft X-ray polarised observation of the Crab PSR and PWN. Our results show that the total polarisation of the pulsed signal is negligible. As can be seen from Fig. 3, the consistency with optical polarisation measure [25] is marginal. Deviations are prominent for Q/I in the left wings of both P1 and P2. U/I on the other hand is in very good agreement. The discrepancy for P1 is an indication that the polarization swing observed in optical, is not fast enough to match the X-ray trend. Note however, that differences are below the 3 σ uncertainty. Only the core of the main peak was found to be significantly polarised. This represents the first statistically significant detection of an X-ray polarized signal from the Crab PSR. Marginal evidence for polarisation, below 3 σ , in other phase bins are also reported. The low average polarization is in contrast with the vast majority of the existing PSR models [33, 34] which typically predict polarisation fraction in the pulsed emission of 40-80%. The model polarisation is generally especially high in the B phase bin. The peaks which are believed to be caustics are typically de-polarised via rapid PA sweeps. In contrast we find our highest PD in the core of P1. Moreover a simple PA swing (at a constant rate over P1) does not seem capable by itself to explain the presence of a highly polarized core in P1 surrounded by low polarization wings, unless the PA swings much faster than in optical. Intrinsic depolarization is most likely required. This is easily seen by comparing the Q/I trend as shown in Fig. 3. Hence the polarization degree must vary across P1, and be intrinsically higher in the core. Analytical striped-wind emission models suggest possible lower polarization in B, but also predict a fully unpolarized P1 [34]. However recent models, focused on emission in the wind and outer magnetosphere, based on numerical magnetospheric solution have shown that the polarization signatures are highly sensitive to the location and geometry of the emission region [35, 36]. Low integrated polarization suggests that the emission region should be close to or beyond the Light Cylinder [36]. However, none of the current models includes important physical ingredients: micro-turbulence, which is likely present in the wind current sheet [37], and could lead to significant depolarization; short time-scale variability which manifests as timing noise and could lead to potential depolarization for long time integration.

A detailed comparison with previous measures, typically in higher energy ranges, or with optical data would benefit from a better statistics, and would require further modeling/extrapolation (to account for changes in the pulse shape with energy) and goes beyond the scope of this work. Thus we have chosen to avoid any discussion/comparison with earlier polarization measurements with statistical significance less than $3\text{-}\sigma$. Due to their large error-bars, previous results [7, 8] are compatible with our measures (see Supplementary Figure 1). The best estimates for the polarised fraction of the hard X-ray integrated PSR emission have values typically $\sim 20\%$ - 30% (with low significance and with some inconsistency among different observations). Given the low MDP (high sensitivity) of our measurement, we can confidently state that the integrated PSR emission in the [2-8] keV must have integrated polarised fraction $<20\%$. Note however, that the more recent PolarLight narrow band [3-4.5] keV measures [10] are consistent with our findings that the PSR emission is likely unpolarized. A strong decrease in the PD of the total pulsed emission, from the optical to the soft X-ray (with a possible recovery to large PD in the hard X-ray) is not expected in existing modeling, which primarily relies on geometry of the emission zone to determine the polarization (e.g. [36]); as noted above, additional physical effects will be required to accommodate the IXPE data.

We were able for the first to map the large scale PWN polarisation pattern confirming the general expectation of a predominantly toroidal magnetic field, extending well beyond the observed location of the X-ray torus. Indeed earlier spatially resolved optical polarization measurements did not show unambiguously the presence of toroidal magnetic field. For synchrotron radiation this is consistent with general expectation from MHD modelling of this source [38–42]. We found however that the mostly symmetric PA (i.e. magnetic field) pattern is associated with large asymmetries in the PD, likely indicating variations in the level of turbulence inside the PWN. Such level of asymmetry is similar to, but stronger than, that seen in the intensity maps, and reflects a similar trend found in optical polarisation images [2].

The magnetic axis of the PWN, derived by taking the symmetry axis of the magnetic field pattern, is found to be $\sim 140^\circ$, about 15° **away** than estimates based on fitting axisymmetric structure to the torus intensity [31]. It is also possible to estimate the inclination of the magnetic axis with respect to the plane of the sky: we found it to be $\sim 60^\circ$, in agreement with previous estimates. While the average PD $\sim 20\%$ agrees with previous measures, the PA differs in a statistically significant way from other estimates, reflecting the spatial variation of the PD, or possible temporal variability. The spatially resolved PD reaches a maximum of $\sim 46\%$ - 50% . This is about two times larger than expected from simple predictions based on synchrotron turbulent modelling of the Crab Torus and Inner Ring luminosity profiles, calibrated on the OSO-8 results [42]. More sophisticate 3D models (lacking however

micro-turbulence) can give PD close to the theoretical maximum $\sim 70\%$ [40], with higher values typically in the South-West region, but in general the prediction is for polarised patterns quite symmetric with respect to the nebular axis, unlike what was found. This suggests that the level and development of turbulence within the nebula, is not as strong as predicted [42] and much patchier in its spatial distribution. While the lower level of polarization close to the center of the PWN is easily explained by summed emission from a wide range of PA in the central resolution elements, the increase of the PD with distance at the rim of the torus suggests the presence of a highly ordered magnetic layer at the edge of the torus itself (the ratio of the energy in the turbulent versus ordered magnetic field components should be about a factor 2 smaller than in the core of the torus [43]). This differs from what is seen in optical where higher polarization is found in a few selected inner features [18], suggesting that optical and X-ray emitting particles might be accelerated in different locations and sample different regions of the nebula as previously suggested [32]. Note however that the X-ray inner ring, which supposedly traces the wind termination shock, at the same distance of the optical wisps (smaller than the IXPE resolution), is strongly subdominant with respect to the torus (and the PSR), such that, even if highly polarized, it would not give a significant signal. The fact that the PD (which depends on the ratio of magnetic energy in the turbulent to ordered components) is far more asymmetric, with respect to the nebular axis, than the intensity (which depends on the total turbulent plus ordered magnetic energy density) suggests that the level of turbulence anti-correlates with the strength of the ordered component of the magnetic field. This is what one would expect if turbulence was driven by the growth of instabilities, like Rayleigh-Taylor, which are suppressed by stronger fields [44]. If this is correct we should expect that more highly polarized PWNe (less turbulent systems) should show a stronger toroidal patterns with smaller degree of Rayleigh-Taylor induced patchy de-polarisation and intensity enhancement.

The IXPE polarisation results indicate that present modeling lacks physical ingredients needed to explain the low pulsar polarisation seen at most phases. The substantial spatial variation of the PD in the nebula also indicates that effects are missing even in the most advanced 3D relativistic Magneto-Hydrodynamical models; MHD turbulence seems likely to be important in both cases.

Methods

3.1 Observations and Data Analysis

The Imaging X-ray Polarimetry Explorer (IXPE), is a NASA mission in partnership with the Italian Space Agency (ASI), launched in December 9 2021. As described in detail elsewhere ([26, 27] and references therein), the IXPE Observatory includes three identical X-ray telescopes (DUs), each comprising a Wolter-I X-ray mirror assembly (NASA-provided) with angular resolution (half-power diameter) of 19 (DU1), 26 (DU2), 28 (DU3) arcsec respectively, and a polarisation-sensitive pixelated detector (GPD, ASI-provided), with a typical energy-dependent dead-time of ~ 1.1 ms. This allows one to measure the energy, arrival direction, arrival time and linear polarization of the detected X-ray signal, which are all reconstructed from the photo-electron track shape using moment analysis. The IXPE energy range is the [2-8] keV band, with a total effective area of 590 cm² at 4.5 keV. The modulation factor (the amplitude of the modulation of the reconstructed photo-electrons angle distribution for a 100% polarised source) ranges from $\sim 15\%$ at 2 keV up to $\sim 60\%$ at 8 keV [27].

The Crab PWN and PSR were observed twice: the first time from 2022-02-21 UTC16:13:32 to 2022-02-22 UTC18:46:37, the second from 2022-03-07 UTC00:14:20 to 2022-03-08 UTC02:40:02, for a total 92363 seconds of ONTIME exposure (the total exposure as obtained from the sum of the good time intervals), and 85062 seconds of total LIVETIME (the total amount of time the CCD was actively observing a source; it excludes the time it takes to transfer charge from the image region to the frame store region).

The polarisation analysis was performed on publicly available level 2 event list files. These were corrected to account for the following calibration issues that have emerged during flight operations. The World Coordinate System (WCS) was corrected to account for the small offset among the various units, registering the pointing solution in order to center the intensity peak of each unit on the PSR position at RA = 5h:34m:31.86s, DEC = 22:00:51.3. The time dependent charge-to-energy conversion was reconstructed for each units using the two onboard calibration sources at 1.7 keV (Si K α) and 5.9 keV (⁵⁵Fe \rightarrow ⁵⁵Mg with following K α emission) [45]. Spurious offsets in the pointing solution (aspect solution), associated to the switch between different star trackers during orbit, were identified looking at the time variations of the count rate in a set of background sky regions, and later filtered out by removing the affected time intervals. This results in a loss of counts smaller than 2% and an effective new on-source time of ~ 91 ks. At the time of the Crab observation, the optical axis of the mirror system relative to the star trackers had not yet been accurately determined and was not yet compensated (by offset pointing). Consequently, the Crab PSR was about 2.8 arcmin off-axis with respect to the mirror system. This precluded accurate computation of

Image Response Functions (IRFs)-energy dependent vignetting and energy dependent exposure maps—necessary for a correct spectral analysis (the mirror-system–star-tracker offset has now been accurately determined and compensated, such that future observations will place the image close to the mirror-system optical axis. Furthermore, it may be possible, in the future, to recalibrate the IRFs), and for computing correct counts rates. However this should not affect polarisation measures which comes from flux ratios among Stokes parameters.

3.2 Timing Analysis

We initially used the Jodrell Bank Crab PSR Monthly ephemeris (<http://www.jb.man.ac.uk/pulsar/crab.html>) [46] to calculate the pulse phase of each photon. However, the time span of the two IXPE observations requires two separate JB solutions, and the alignment between the arrival time of the pulse in the two observations using these ephemerides is visibly off (~ 0.02 in phase). Therefore, we determined a new ephemeris by using the X-ray data alone, as follows. As a starting point, we used the JB montly ephemeris of February in CGRO format (https://www.jb.man.ac.uk/~pulsar/crab/CGRO_format.html), but modifying the frequency and derivatives in order for them to refer to an epoch between the two observations:

$$\nu_{\text{new}} = \nu_{\text{old}} + \dot{\nu}_{\text{old}}(T_{\text{new}} - T_{\text{old}}) + 0.5\ddot{\nu}_{\text{old}}(T_{\text{new}} - T_{\text{old}})^2 \quad (1)$$

$$\dot{\nu}_{\text{new}} = \dot{\nu}_{\text{old}}(T_{\text{new}} - T_{\text{old}}) \quad (2)$$

where ν_{old} , $\dot{\nu}_{\text{old}}$, and $\ddot{\nu}_{\text{old}}$ are the frequency, its first and second time derivative at T_{old} , while ν_{new} , $\dot{\nu}_{\text{new}}$ are the frequency and its first time derivative at T_{new} .

Then, we calculated times of arrival (TOAs) of the pulse using the `HENphaseogram` tool distributed with `HENDRICS` (<https://hendrics.stingray.science>) [47]. This tool folds the data in small fractions of the observation, creating a series of pulse profiles. Then, it calculates the misalignment between each of these profiles and a smoothed version of the folded profile from the whole observation, and transforms this misalignment into a TOA. The TOA refers to the maximum of the reference profile. As an output, the tool produces a parameter file and a TOA file in `Tempo2` format [48]. We loaded these approximate parameters and TOAs in the `pink` graphical interface to `PINT` (<https://nanograv-pint.readthedocs.io>) [49], and fitted a new spin down solution that aligned the TOAs of the two observations. Then, we went back and calculated new TOAs, this time using the improved timing solution and, consequently, the better resolved total pulse profile that the solution provided, and fitted these TOAs again with `PINT`. We stopped this iterative procedure when the improvement in the fitting through `PINT` was smaller than the uncertainties. Finally, we calculated the closest TOA

to the epoch chosen for the timing solution, and referred the frequency and derivatives to this time, using the above equation, in order to have a single number for the reference TOA and the PEPOCH of the timing solution for convenience. The new ephemeris is reported in Supplementary Table 1. Note that, having chosen the reference time in between the February and March observations, the determination of the second time derivative of the period is highly uncertain, but on the other hand the correction due to the second time derivative is not significant, and can potentially be neglected. Note moreover that the absolute time alignment of the pulse profile is not necessary for the analysis in this Paper. However we did verify that the X-ray pulse leads the radio pulse (as provided by the JB ephemeris) by $\sim 300 \mu\text{s}$, consistent with past observations from other missions [50, e.g.]. The Crab pulsar is a young one and his timing can be quite noisy, to the point that ephemeris cannot be extended beyond their range of validity.

3.3 Polarization Analysis

The polarisation analysis of both the PWN and the PSR was performed using the IXPE collaboration software `ixpeobssim` V26.3.2. `ixpeobssim` has been designed to act both as a simulation software and for data reduction. We opted for a more robust and established unweighted analysis, limited to the [2-8] keV energy range. Phase folding was performed with `xpphase`, while event selection was done using the `xpselect` tool. Polarization was computed with the `xpbin` tool and PCUBE and PMAPCUBE methods.

Given the additive nature of Stokes parameters, in order to get the polarization properties of a spatial region and/or phase range of interest, one just need to take the sum of U and Q of each event (calibrated for the known spurious modulation of the instrument, and corrected for the modulation factor [27]) within the same region and/or phase range. `ixpeobssim` can compute all polarisation relevant quantities including their error and the significance. Deformation of the phase-resolved light curve (pulse shape) due to dead time, with respect to the dead-time corrected one, is estimated to be less than 3% [difference between the dead time correction when the count rate is at maximum (P1) and the one when the count rate is at minimum (OP)], and was thus ignored. The net PSR's Stokes parameters in a given phase bin are obtained as follows: for a generic Stokes parameter X (=I,U,Q) of phase bin i we have $X_{op-sub,i} = X_{tot,i} - X_{op}(\Delta_{phase,i}/\Delta_{phase,op})$, where $\Delta_{phase,i}$ is the phase width of phase bin i and $\Delta_{phase,op}$ is the phase width of OP bin (0.3). Supplementary Figure 4 shows the maps of normalized Stokes parameters, of the total PWN plus PSR emission. The contribution of the lowly polarised PSR is hardly visible. We verified that the pattern, apart from counting noise, is the same if one considers just the emission in the OP phase range. While the U/I map shows a high level of symmetry with respect to the direction of the nebular axis inferred from the intensity maps [31], the one for Q/I is far more asymmetric (its symmetry axis is more aligned with the North-South

direction). The inclination of the magnetic axis of the nebula was derived by fitting ellipses to the internal magnetic field structure as displayed in Figure 4.

Due to the brightness of the Crab Complex, all the IXPE field of view contains events from the PSR and PWN, however, for space integrated measures, we have verified that polarization properties do not change once one selects a circular region centered on the PSR and with radius > 2 arcmin (we selected 2.5 arcmin). Supplementary Figure 5 shows that $\sim 98\%$ of counts are within 2 arcmin. For the PSR analysis we have verified, using a large set of mocked observations, that the optimal region size, in order to reduce the errors of the OP-subtracted polarization measures, ranges between 15 and 25 arcsec. We opted for 20 arcsec. See also Supplementary Figure 5.

We caution the reader that due to error in the reconstruction of the photons absorption point in the Gas Pixel Detector (GPD), polarisation leakage can contaminate the Stokes maps. The effect of polarization leakage, arises specifically from correlations between the reconstructed polarization angle and the photon absorption point in the GPD. This leads to false polarisation patterns (this has no effect on integrated or OP subtracted values), even for unpolarized sources. Preliminary estimates based on Montecarlo simulations of the GPD response, indicate that this effect can at most be as high as 10% in the outer regions of the PWN, and does not alter significantly our overall findings. A more detailed discussion and treatment of this effect will be presented in a forthcoming publication.

3.4 CHANDRA Observation

The Crab PWN was observed by CHANDRA (OsbID 23539) starting on 2022-03-15 at 11:32:23 UTC and ending on 2022-03-15 at 15:14:17 UTC, for a total of $\sim 10^4$ seconds; due to telemetry saturation from the bright source, the effective exposure time was 1331 seconds. Data were processed with the CIAO package 4.14 using CALDB 4.9.7, with the `chandra repro mode=h` tool using default settings, and the [2-8] keV image was done with the `fluximage` tool, and later smoothed with a gaussian kernel using `aconvolve kernelspec='lib:gaus(2,5,1,1,1)'`

Supplementary information. Supplementary material includes Figures 1 to 5, and Tables 1 to 2.

Data Availability. Data of the Crab pulsar and nebula observation are available in the HEASARC IXPE Data Archive (<https://heasarc.gsfc.nasa.gov/docs/ixpe/archive/>).

Code Availability. The `ixpeobssim` software and documentation can be downloaded at: <https://github.com/lucabaldini/ixpeobssim>. Other information supporting the findings of this study, and specific data-reduction pipelines, are available from the corresponding authors upon request.

Acknowledgments. The Imaging X-ray Polarimetry Explorer (IXPE) is a joint US and Italian mission. The US contribution is supported by the National Aeronautics and Space Administration (NASA) and led and managed by its Marshall Space Flight Center (MSFC), with industry partner Ball Aerospace (contract NNM15AA18C). The Italian contribution is supported by the Italian Space Agency (Agenzia Spaziale Italiana, ASI) through contract ASI-OHBI-2017-12-I.0, agreements ASI-INAF-2017-12-H0 and ASI-INFN-2017.13-H0, and its Space Science Data Center (SSDC) with agreements ASI-INAF-2022-14-HH.0 and ASI-INFN 2021-43-HH.0, and by the Istituto Nazionale di Astrofisica (INAF) and the Istituto Nazionale di Fisica Nucleare (INFN) in Italy. This research used data products provided by the IXPE Team (MSFC, SSDC, INAF, and INFN) and distributed with additional software tools by the High-Energy Astrophysics Science Archive Research Center (HEASARC), at NASA Goddard Space Flight Center (GSFC). The research at Boston University was supported in part by National Science Foundation grant AST-2108622. Part of the French contributions is supported by the Scientific Research National Center (CNRS) and the French spatial agency (CNES). I. Agudo acknowledges financial support from the Spanish "Ministerio de Ciencia e Innovación through the "Center of Excellence Severo Ochoa" award for the Instituto de Astrofísica de Andalucía-CSIC (SEV-2017-0709), and through grants AYA2016-80889-P and PID2019-107847RB-C44. C.-Y. Ng and Y. J. Yang are supported by a GRF grant of the Hong Kong Government under HKU 17305419. N. Bucciantini was supported by the INAF MiniGrant "PWNumpol - Numerical Studies of Pulsar Wind Nebulae in The Light of IXPE".

Author contributions. NB led the data analysis and the writing of the paper. RF, MB, JR, LP, FM contributed to data analysis and data calibration. NDL, CS, NO, TK, TM, SG, EW contributed to data analysis and results interpretation. MCW, MN, SS, EDOW, FX, JH, RWR, PT, AP, HLM contributed to text revision, and data interpretation. LB and MPR contribute to software development. The remaining members of the IXPE collaboration contributed to the design of the mission, to the calibration of the instrument, to define its science case and to the planning of the observations. All authors provided inputs and comments on the manuscript.

Competing interests. Authors declare that they have no competing interests.

Table 1: Global polarisation properties of the PSR+PWN complex. Normalized Stokes parameters, Polarised Degree and Angle for various energy and phase ranges (in brackets the 1σ errors). The OP is in the [2-8] keV range. The significance (Sig) is given as the ratio of PD over its 1σ error. See Figure 1

Selection	Q/I	U/I	PD[%]	PA[deg]	Sig
PSR+PWN [2-8] keV	0.177(0.0019)	0.068(0.0019)	19.0(0.19)	145.5(0.29)	99
PSR+PWN [2-4] keV	0.168(0.0019)	0.081(0.0019)	18.7(0.19)	147.8(0.29)	100
PSR+PWN [4-8] keV	0.199(0.0038)	0.037(0.0039)	20.2(0.38)	140.2(0.55)	53
PWN (Off Pulse)	0.189(0.0036)	0.073(0.0036)	20.2(0.36)	145.6(0.51)	57

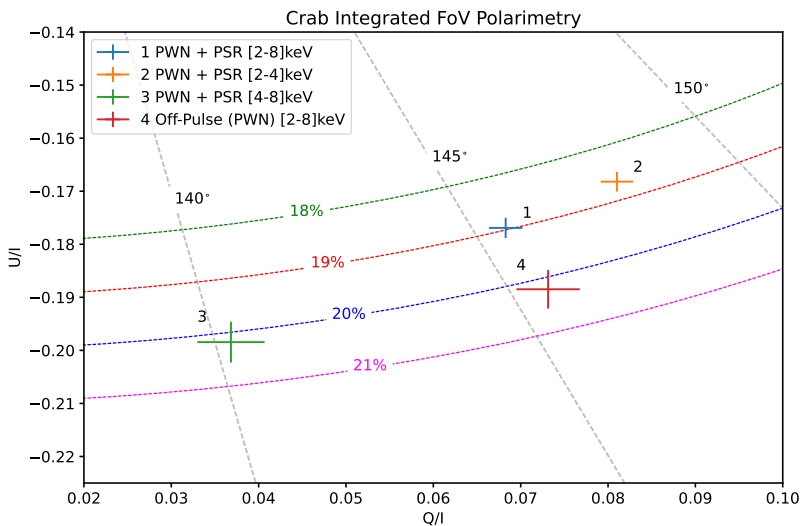


Fig. 1: Global Polarisation properties of the Crab PWN+PSR complex. Emission is integrated over a region of $2.5'$ radius centered on the PSR. Normalized Stokes parameters are shown for the total emission, the emission in the [2-4] keV and [4-8] keV energy bands (mean values plus error-bars representing the 1σ standard deviation), and for the OP only, together with contours of polarised degree (in %) and angle.

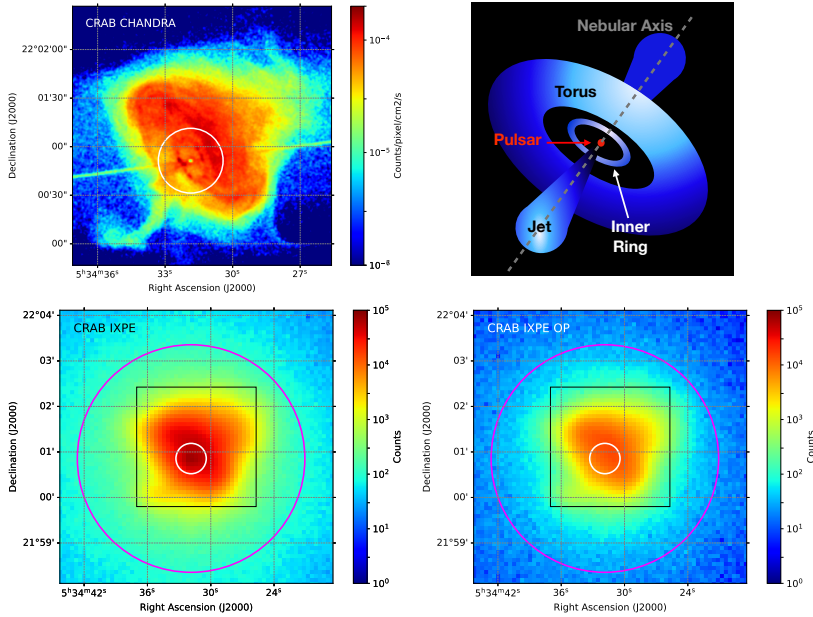


Fig. 2: Comparison of Chandra and IXPE images. Top Left panel: Chandra image (ObdID 23539) (intensity map) of the Crab PWN in the [2-8] keV energy range. Top Right panel: cartoon of the jet-torus structure indicating the main features observed in X-rays. Bottom Left panel: Total IXPE count map in the [2-8] keV energy range. Bottom Right panel: OP (see the Supplementary Materials for the definition of its phase range) only IXPE count map in the [2-8] keV energy range. The white circular region of 20'' radius is the one used to do the phase-resolved polarimetry of the PSR, the magenta circular region of 2.5 arcmin radius is the one used for spatially integrated measures. The black box represents the region corresponding to the Chandra image.

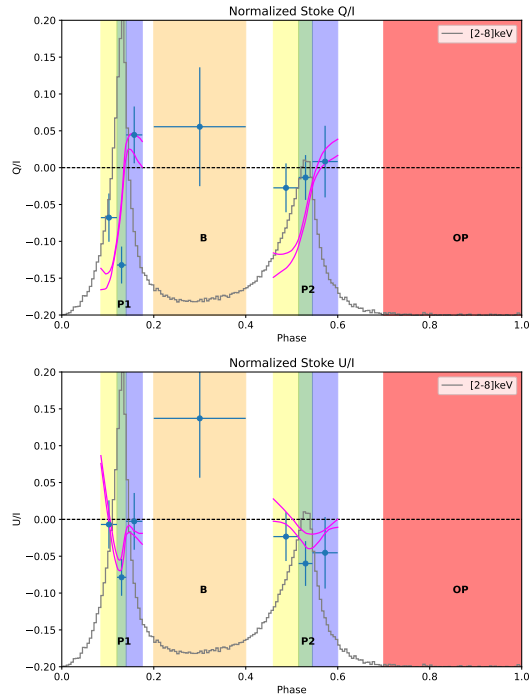


Fig. 3: Polarization properties of the Crab PSR. Normalized Stokes Parameters (means with vertical bar for their 1σ standard deviation) for the OP subtracted emission of the Crab PSR in the [2-8] keV energy bands (blue crosses - horizontal bar is the bin width), overlaid with the phase bins of interest: OP (red), P1 and P2 centers (green), left wings (yellow) and right wings (blue), and B (orange) (see the Supplementary Materials for the definition of the various phase ranges). Overlaid is the OP subtracted PSR light curve (counts) in the [2-8] keV energy band, normalised and rescaled to the range of the y-axis (grey solid line). The magenta curves represent the range of optical data [25] over P1 and P2.

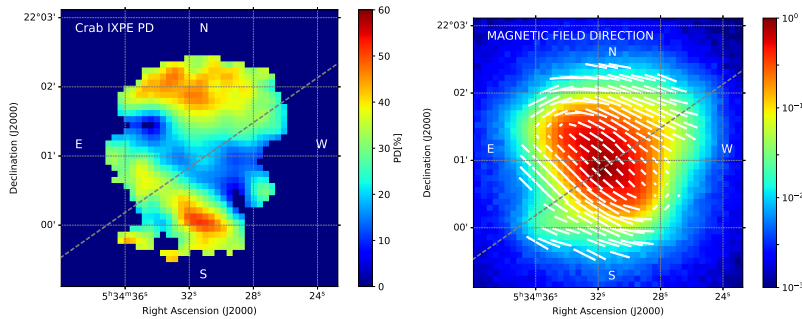


Fig. 4: Polarized Structure of the Crab nebula. Right panel: Total intensity map of the Crab PWN+PSR complex in the [2–8] keV energy band, overlaid with the reconstructed polarisation direction (magnetic field). Left panel: map of the polarization degree cut above 5σ confidence level. The gray dashed line is the nebular axis inferred from X-ray intensity maps [31]. Overlaid are the Sky directions for ease of reference.

References

- [1] Gaensler, B. M. & Slane, P. O. The Evolution and Structure of Pulsar Wind Nebulae. *Annu. Rev. Astron. Astrophys.* **44**, 17–47 (2006). <https://doi.org/10.1146/annurev.astro.44.051905.092528>, <https://arxiv.org/abs/arXiv:astro-ph/0601081>.
- [2] Hester, J. J. The Crab Nebula: An Astrophysical Chimera. *Annu. Rev. Astron. Astrophys.* **46**, 127–155 (2008). <https://doi.org/10.1146/annurev.astro.45.051806.110608>.
- [3] Weisskopf, M. C., Silver, E. H., Kestenbaum, H. L., Long, K. S. & Novick, R. A precision measurement of the X-ray polarization of the Crab Nebula without pulsar contamination. *Astrophys. J. Lett.* **220**, L117–L121 (1978). <https://doi.org/10.1086/182648>.
- [4] Forot, M., Laurent, P., Grenier, I. A., Gouiffès, C. & Lebrun, F. Polarization of the Crab Pulsar and Nebula as Observed by the INTEGRAL/IBIS Telescope. *Astrophys. J. Lett.* **688**, L29–L32 (2008). <https://doi.org/10.1086/593974>, <https://arxiv.org/abs/0809.1292>.
- [5] Moran, P. *et al.* Optical polarimetry of the inner Crab nebula and pulsar. *Mon. Not. R. Astron. Soc.* **433**, 2564–2575 (2013). <https://doi.org/10.1093/mnras/stt931>, <https://arxiv.org/abs/1305.6824> [astro-ph.HE].
- [6] Chauvin, M., Roques, J. P., Clark, D. J. & Jourdain, E. Polarimetry in the Hard X-Ray Domain with INTEGRAL SPI. *Astrophys. J.* **769** (2), 137 (2013). <https://doi.org/10.1088/0004-637X/769/2/137>,

- <https://arxiv.org/abs/1305.0802> [astro-ph.IM].
- [7] Chauvin, M. *et al.* Shedding new light on the Crab with polarized X-rays. *Sci. Rep.* **7**, 7816 (2017). <https://doi.org/10.1038/s41598-017-07390-7>, <https://arxiv.org/abs/1706.09203> [astro-ph.HE].
- [8] Vadawale, S. V. *et al.* Phase-resolved X-ray polarimetry of the Crab pulsar with the AstroSat CZT Imager. *Nat. Astron.* **2**, 50–55 (2018). <https://doi.org/10.1038/s41550-017-0293-z> .
- [9] Feng, H. *et al.* Re-detection and a possible time variation of soft X-ray polarization from the Crab. *Nat. Astron.* **4**, 511–516 (2020). <https://doi.org/10.1038/s41550-020-1088-1>, <https://arxiv.org/abs/2011.05487> [astro-ph.HE].
- [10] Long, X. *et al.* X-Ray Polarimetry of the Crab Nebula with PolarLight: Polarization Recovery after the Glitch and a Secular Position Angle Variation. *Astrophys. J. Lett.* **912** (2), L28 (2021). <https://doi.org/10.3847/2041-8213/abfb00>, <https://arxiv.org/abs/2104.11391> [astro-ph.HE].
- [11] Li, H.-C. *et al.* Gamma-ray polarimetry of the Crab pulsar observed by POLAR. *Mon. Not. R. Astron. Soc.* **512** (2), 2827–2840 (2022). <https://doi.org/10.1093/mnras/stac522>, <https://arxiv.org/abs/2202.10877> [astro-ph.HE].
- [12] Trimble, V. The Distance to the Crab Nebula and NP 0532. *Publ. Astron. Soc. Pac.* **85** (507), 579 (1973). <https://doi.org/10.1086/129507> .
- [13] Kargaltsev, O. & Pavlov, G. G. C. Bassa, Z. Wang, A. Cumming, & V. M. Kaspi (ed.) *Pulsar Wind Nebulae in the Chandra Era*. (ed. C. Bassa, Z. Wang, A. Cumming, & V. M. Kaspi) *40 Years of Pulsars: Millisecond Pulsars, Magnetars and More*, Vol. 983 of *Am. Inst. Phys. Conf. Ser.*, 171–185 (2008). [0801.2602](https://doi.org/10.1063/1.2900000).
- [14] Mori, K. *et al.* Spatial Variation of the X-Ray Spectrum of the Crab Nebula. *Astrophys. J.* **609**, 186–193 (2004). <https://doi.org/10.1086/421011>, <https://arxiv.org/abs/arXiv:astro-ph/0403287> .
- [15] Hester, J. J. *et al.* WFPC2 Studies of the Crab Nebula. I. HST and ROSAT Imaging of the Synchrotron Nebula. *Astrophys. J.* **448**, 240–263 (1995). <https://doi.org/10.1086/175956> .
- [16] Weisskopf, M. C. *et al.* Discovery of Spatial and Spectral Structure in the X-Ray Emission from the Crab Nebula. *Astrophys. J. Lett.* **536**, L81–L84 (2000). <https://doi.org/10.1086/312733>, <https://arxiv.org/abs/arXiv:astro-ph/0003216> .

- [17] Aumont, J. *et al.* Measurement of the Crab nebula polarization at 90 GHz as a calibrator for CMB experiments. *Astron. Astrophys.* **514**, A70 (2010). <https://doi.org/10.1051/0004-6361/200913834>, <https://arxiv.org/abs/0912.1751> .
- [18] Moran, P. *et al.* Optical polarimetry of the inner Crab nebula and pulsar. *Mon. Not. R. Astron. Soc.* **433**, 2564–2575 (2013). <https://doi.org/10.1093/mnras/stt931>, <https://arxiv.org/abs/1305.6824> [astro-ph.HE].
- [19] Zanin, R. Torres, D. F. (ed.) *Crab Observational Status: Nebulae, Pulsations, and Flares.* (ed. Torres, D. F.) *Modelling Pulsar Wind Nebulae*, Vol. 446 of *Astrophys. Space Sci. Lib.*, 101 (2017).
- [20] Kaaret, P. *et al.* Chandra Observations of the Young Pulsar PSR B0540-69. *Astrophys. J.* **546** (2), 1159–1167 (2001). <https://doi.org/10.1086/318287>, <https://arxiv.org/abs/astro-ph/0008388> [astro-ph].
- [21] Massaro, E., Campana, R., Cusumano, G. & Mineo, T. The optical to γ -ray emission of the Crab pulsar: a multicomponent model. *Astron. Astrophys.* **459** (3), 859–870 (2006). <https://doi.org/10.1051/0004-6361:20065118>, <https://arxiv.org/abs/astro-ph/0607410> [astro-ph].
- [22] Weisskopf, M. C. *et al.* Chandra Phase-resolved X-Ray Spectroscopy of the Crab Pulsar. *Astrophys. J.* **743** (2), 139 (2011). <https://doi.org/10.1088/0004-637X/743/2/139>, <https://arxiv.org/abs/1106.3270> [astro-ph.GA].
- [23] Ge, M. Y. *et al.* X-Ray Phase-resolved Spectroscopy of PSRs B0531+21, B1509-58, and B0540-69 with RXTE. *Astrophys. J. Suppl. Ser.* **199**, 32 (2012). <https://doi.org/10.1088/0067-0049/199/2/32>, <https://arxiv.org/abs/1204.2199> [astro-ph.HE].
- [24] Vivekanand, M. Phase-resolved spectrum of the Crab pulsar from NICER. *Astron. Astrophys.* **649**, A140 (2021). <https://doi.org/10.1051/0004-6361/202140358>, <https://arxiv.org/abs/2102.04675> [astro-ph.HE].
- [25] Słowikowska, A., Kanbach, G., Kramer, M. & Stefanescu, A. Optical polarization of the Crab pulsar: precision measurements and comparison to the radio emission. *Mon. Not. R. Astron. Soc.* **397** (1), 103–123 (2009). <https://doi.org/10.1111/j.1365-2966.2009.14935.x>, <https://arxiv.org/abs/0901.4559> [astro-ph.SR].
- [26] Weisskopf, M. *The Imaging X-ray Polarimetry Explorer (IXPE) Mission Overview*, Vol. 54 of *Am. Astr. Soc. High En. Div.*, 301.01 (2022).
- [27] Weisskopf, M. C. *et al.* Imaging X-ray Polarimetry Explorer: prelaunch. *J. Astron. Telesc. Instrum. Syst.* **8** (2), 1 – 28 (2022). URL <https://>

- doi.org/10.1117/1.JATIS.8.2.026002. <https://doi.org/10.1117/1.JATIS.8.2.026002> .
- [28] Pesce-Rollins, M., Lalla, N. D., Omodei, N. & Baldini, L. An observation-simulation and analysis framework for the Imaging X-ray Polarimetry Explorer (IXPE). *Nucl. Inst. and Meth. in Phys. Res. A* **936**, 224–226 (2019). <https://doi.org/10.1016/j.nima.2018.10.041> .
- [29] Baldini, L. *et al.* ixpeobssim: a Simulation and Analysis Framework for the Imaging X-ray Polarimetry Explorer. *arXiv e-prints* arXiv:2203.06384 (2022). <https://arxiv.org/abs/2203.06384> [astro-ph.IM].
- [30] Tennant, A. F. *et al.* Discovery of X-Ray Emission from the Crab Pulsar at Pulse Minimum. *Astrophys. J. Lett.* **554** (2), L173–L176 (2001). <https://doi.org/10.1086/321718> .
- [31] Ng, C.-Y. & Romani, R. W. Fitting Pulsar Wind Tori. *Astrophys. J.* **601**, 479–484 (2004). <https://doi.org/10.1086/380486>, <https://arxiv.org/abs/astro-ph/0310155> .
- [32] Schweizer, T. *et al.* Characterization of the optical and X-ray properties of the north-western wisps in the Crab nebula. *Mon. Not. R. Astron. Soc.* **433**, 3325–3335 (2013). <https://doi.org/10.1093/mnras/stt995>, <https://arxiv.org/abs/1301.1321> [astro-ph.HE].
- [33] Dyks, J. & Harding, A. K. Rotational Sweepback of Magnetic Field Lines in Geometric Models of Pulsar Radio Emission. *Astrophys. J.* **614** (2), 869–880 (2004). <https://doi.org/10.1086/423707>, <https://arxiv.org/abs/astro-ph/0402507> [astro-ph].
- [34] Pétri, J. Phase-resolved polarization properties of the pulsar striped wind synchrotron emission. *Mon. Not. R. Astron. Soc.* **434** (3), 2636–2644 (2013). <https://doi.org/10.1093/mnras/stt1214>, <https://arxiv.org/abs/1308.0973> [astro-ph.HE].
- [35] Cerutti, B., Mortier, J. & Philippov, A. A. Polarized synchrotron emission from the equatorial current sheet in gamma-ray pulsars. *Mon. Not. R. Astron. Soc.* **463** (1), L89–L93 (2016). <https://doi.org/10.1093/mnrasl/slwl62>, <https://arxiv.org/abs/1609.00021> [astro-ph.HE].
- [36] Harding, A. K. & Kalapotharakos, C. Multiwavelength Polarization of Rotation-powered Pulsars. *Astrophys. J.* **840** (2), 73 (2017). <https://doi.org/10.3847/1538-4357/aa6ead>, <https://arxiv.org/abs/1704.06183> [astro-ph.HE].

- [37] Cerutti, B., Philippov, A. A. & Dubus, G. Dissipation of the striped pulsar wind and non-thermal particle acceleration: 3D PIC simulations. *Astron. Astrophys.* **642**, A204 (2020). <https://doi.org/10.1051/0004-6361/202038618>, <https://arxiv.org/abs/2008.11462> [astro-ph.HE].
- [38] Bucciantini, N., del Zanna, L., Amato, E. & Volpi, D. Polarization in the inner region of pulsar wind nebulae. *Astron. Astrophys.* **443**, 519–524 (2005). <https://doi.org/10.1051/0004-6361:20053667>, <https://arxiv.org/abs/arXiv:astro-ph/0508212> .
- [39] Nakamura, Y. & Shibata, S. Polarization of the Crab Nebula with disordered magnetic components. *Mon. Not. R. Astron. Soc.* **381**, 1489–1498 (2007). <https://doi.org/10.1111/j.1365-2966.2007.12172.x>, <https://arxiv.org/abs/arXiv:astro-ph/0702512> .
- [40] Porth, O., Komissarov, S. S. & Keppens, R. Three-dimensional magnetohydrodynamic simulations of the Crab nebula. *Mon. Not. R. Astron. Soc.* **438**, 278–306 (2014). <https://doi.org/10.1093/mnras/stt2176>, <https://arxiv.org/abs/1310.2531> [astro-ph.HE].
- [41] Olmi, B., Del Zanna, L., Amato, E., Bucciantini, N. & Mignone, A. Multi-D magnetohydrodynamic modelling of pulsar wind nebulae: recent progress and open questions. *J. Plas. Phys.* **82** (6), 635820601 (2016). <https://doi.org/10.1017/S0022377816000957>, <https://arxiv.org/abs/1610.07956> [astro-ph.HE].
- [42] Bucciantini, N., Bandiera, R., Olmi, B. & Del Zanna, L. Modeling the effect of small-scale magnetic turbulence on the X-ray properties of Pulsar Wind Nebulae. *Mon. Not. R. Astron. Soc.* **470**, 4066–4074 (2017). <https://doi.org/10.1093/mnras/stx993>, <https://arxiv.org/abs/1704.06546> [astro-ph.HE].
- [43] Bandiera, R. & Petruk, O. Radio polarization maps of shell-type supernova remnants - I. Effects of a random magnetic field component and thin-shell models. *Mon. Not. R. Astron. Soc.* **459**, 178–198 (2016). <https://doi.org/10.1093/mnras/stw551>, <https://arxiv.org/abs/1603.01199> [astro-ph.HE].
- [44] Bucciantini, N., Amato, E., Bandiera, R., Blondin, J. M. & Del Zanna, L. Magnetic Rayleigh-Taylor instability for Pulsar Wind Nebulae in expanding Supernova Remnants. *Astron. Astrophys.* **423**, 253–265 (2004). <https://doi.org/10.1051/0004-6361:20040360>, <https://arxiv.org/abs/arXiv:astro-ph/0405276> .
- [45] Ferrazzoli, R. *et al.* In-flight calibration system of imaging x-ray polarimetry explorer. *J. Astron. Telesc. Instrum. Syst.* **6**, 048002 (2020). <https://doi.org/10.1117/1.JATIS.6.4.048002>, <https://arxiv.org/>

- [abs/2010.14185](#) [astro-ph.IM].
- [46] Lyne, A. G., Pritchard, R. S. & Graham-Smith, F. Twenty-Three Years of Crab Pulsar Rotational History. *Mon. Not. R. Astron. Soc.* **265**, 1003–+ (1993) .
- [47] Bachetti, M. HENDRICS: High ENergy Data Reduction Interface from the Command Shell. Astrophysics Source Code Library, record ascl:1805.019 (2018). [1805.019](#).
- [48] Hobbs, G. B., Edwards, R. T. & Manchester, R. N. TEMPO2, a new pulsar-timing package - I. An overview. *Mon. Not. R. Astron. Soc.* **369** (2), 655–672 (2006). <https://doi.org/10.1111/j.1365-2966.2006.10302.x>, <https://arxiv.org/abs/astro-ph/0603381> [astro-ph].
- [49] Luo, J. *et al.* PINT: A Modern Software Package for Pulsar Timing. *Astrophys. J.* **911** (1), 45 (2021). <https://doi.org/10.3847/1538-4357/abe62f>, <https://arxiv.org/abs/2012.00074> [astro-ph.IM].
- [50] Kuiper, L., Hermsen, W., Walter, R. & Foschini, L. Absolute timing with IBIS, SPI and JEM-X aboard INTEGRAL. Crab main-pulse arrival times in radio, X-rays and high-energy gamma -rays. *Astron. Astrophys.* **411**, L31–L36 (2003). <https://doi.org/10.1051/0004-6361:20031353>, <https://arxiv.org/abs/astro-ph/0309178> [astro-ph].